Nanoscale

Gauging surface charge distribution of live cell membrane by ionic current change using scanning ion conductance microscopy

Journal:	*Nanoscale*
Manuscript ID	NR-ART-08-2021-005230.R2
Article Type:	Paper
Date Submitted by the Author:	31-Oct-2021
Complete List of Authors:	Chen, Feng; Nanjing Medical University He, Jin; Florida International University, Physics department Manandhar, Prakash; Florida International University Yang, Yizi; Nanjing Medical University Liu, Peidang; Southeast University Gu, Ning; Southeast University, School of Biological Science and Medical Engineering

ARTICLE

Gauging surface charge distribution of live cell membrane by ionic current change using scanning ion conductance microscopy

Received 00th January 20xx,
Accepted 00th January 20xx

DOI: 10.1039/x0xx00000x

*Feng Chen[a, b], Jin He[*b], Prakash Manandhar[c], Yizi Yang[a], Peidang Liu[d], Ning Gu [*a, d]*

The distribution of surface charge and potential of cell membrane plays an indispensable role in cellular activities. However, probing surface charge of live cells in physiological conditions, until recently, remains an arduous challenge owing to lack of effective methods. Scanning ion conductance microscope (SICM) is an emerging imaging technique for imaging live cell membrane in its native state. Here, we introduce a simple SICM based imaging technique to effectively map the surface charge contrast distribution of soft substrates including cell membrane by utilizing the higher surface charge sensitivity of the ionic current when the nanopipette tip is close to the substrate with a relatively high current change. This technique was assessed on charged model substrates made by polydimethylsiloxane, and the surface charge sensitivity of ionic current change was supported by finite element method simulations. With this method, we can distinguish the surface charge difference between cell membrane and the supporting collagen matrix. We also observed the surface charge change induced by the small membrane damage after 1% dimethyl sulfoxide (DMSO) treatment. This new SICM technique provides opportunities to study interfacial and cell membrane processes with high spatial resolution.

1. Introduction

The surface charge and surface potential are the intrinsic properties of cell membrane and the microscopic distributions play profound roles in important cellular activities, such as cell signalling process, cell-cell communication, and tissue formation.[1-3] The optical microscope-based techniques, especially fluorescence microscopes, are powerful and widely used in cell and tissue imaging. However, the electrostatic and electrochemical properties of cell membrane are still difficult to be imaged with sufficient spatial and time resolutions.[2, 4] As a surface imaging technique, atomic force microscopy (AFM) based methods can perform imaging of surface potential/charge distribution in various types of biological sample at a sub-nanometer resolution. Kelvin probe force microscopy (KFM) can perform nanoscale imaging of surface potential by the measurement of contact potential difference between probe and sample.[5, 6] Electrostatic force microscopy (EFM) has been applied in characterization of charge distribution, charge density and charge migration in various biological samples.[7, 8] However, these measurements can only work in harsh conditions and the physical contact between scanning probe and sample surface inevitably impairs the delicate surface of sample.[5, 9, 10] Another scanning probe microscopy method, scanning ion conductance microscopy (SICM)[11, 12] has emerged as a powerful imaging technique for non-invasive topographical mapping of the live cell membrane with nanoscale resolution in physiological environments and has been used to monitor the dynamic changes of cell membrane induced by various cellular activities, such as life cycle and endocytosis, and by the exposure to external stimulus, such as virus and nanoparticles.[13-20] In SICM, the scanning probe is an electrolyte-filled pipette with a sub-microscale to nanoscale opening at the tip orifice, which was pulled from glass or quartz capillaries.[21] As the nanopipette tip approaches close to sample, the ion current changes quickly and is proportional to the probe-sample distance (D_{ps}), which is used as the feedback signal to control the D_{ps}. This technique does not require a direct physical contact between scanning probe and sample, thus minimizing the disturbance to imaged surface. The ionic current feedback is robust and researchers have confirmed that the changes of membrane can be tracked using SICM for days in a stable environment.[13, 14, 22, 23]

The ionic current response in SICM is inherently sensitive to the variations of local electrostatic environment in the region between nanopipette tip and sample. These variations may be caused by surface charge/potential heterogeneities, ion concentration gradient, surface reactions, and other interfacial processes.[24-27] In principle, the ionic current can be utilized for surface charge mapping if we can better deconvolute the

[a] School of Biomedical Engineering and Informatics, Nanjing Medical University, Nanjing 211166, People's Republic of China
[b] Physics Department, Biomolecular Science Institute, Florida International University, Miami, FL 33199, United States
[c] Department of Chemistry and Biochemistry, Florida International University, Miami, FL 33199, United States
[d] Jiangsu Key Laboratory for Biomaterials and Devices, School of Biological Science and Medical Engineering, Southeast University, Nanjing 210009, China
Email: jinhe@fiu.edu; guning@esu.edu.cn
Electronic Supplementary Information (ESI) available: [details of any supplementary information available should be included here]. See DOI: 10.1039/x0xx00000x

contribution of surface charge to ionic current change. Compared with fluorescence methods, SICM is expected to reveal the surface charge/potential of non-labelled living cell with higher spatial resolution.[21] In recent years, there are several works to advance the surface charge/potential mapping capability of SICM. McKelvey *et al*. reported the first method to image surface charge based on the phase shifts observed in the distance-modulated mode.[28] A bias modulated SICM was also demonstrated to simultaneously acquire both the topography and charge distribution of cell surface, and the surface charge maps were generated with the support of simulations.[29, 30] The same group also developed a simplified method, differential-concentration SICM, to map the surface charge of PC12 cells.[24] Klausen *et al.* obtained the topographical images of lipid bilayers at both positive and negative biases, and the difference of the two topography images revealed the surface charge distributions of the lipid membrane, which would be difficult to capture the dynamic changes of cell membranes.[31] Instead of current detection, a surface charge imaging method based on potentiometric measurement was demonstrated by distinguishing nanopores of a porous membrane through surface potential mapping.[32] We recently also developed a simplified potentiometric SICM method for simultaneous topography and surface potential imaging of live cell membranes by recording both current and open-circuit potential (OCP) signals.[21, 33] However, both the current and OCP signals needed to be recorded simultaneously and the imaging speed is relatively slow.

These recent progresses suggest the development of surface charge/potential imaging methods for live cell membrane based on SICM is promising. Obviously, the development is still in the early stage and each method has its own advantages and disadvantages. In this work, we developed a simple method to map the surface charge contrast by directly using the ionic current change at each pixel in approach-retract scan (ARS) mode (also called hopping mode).[34, 35] Based on single point approach-withdraw measurements and the numerical simulations by Finite Element Method (FEM), the current change is more sensitive to the surface charge of substrate when the tip is closer to the substrate. To enhance the sensitivity of ionic current change to surface charge, we allow bigger change in current by using a relatively fast scanning speed. The larger current change ΔI_f during the ARS fine scans is utilized for surface charge contrast mapping. We tested the surface charge sensing capability of this method by using charged polydimethylsiloxane (PDMS) substrates. The soft PDMS substrate can protect the nanopipette tip even when the tip is very close to the surface, and the tip is also flexible enough to minimize the damage to sample surface. The closest distance of the tip to sample can still be controlled reasonably well, and the topography image can be acquired without obvious distortions and significant artifacts. The ΔI_f-based SICM method worked reasonably well on rougher gold deposited PDMS substrates. This new method was then utilized to map the surface charge contrast distribution of live cell membrane and we could distinguish small changes of cell membrane induced by dimethyl sulfoxide (DMSO) treatment. These measurements serve to illustrate an effective gauge of imaging interfacial properties besides topography with the use of ΔI_f-based SICM. The extracellular surface charge distribution of live cell membrane can be used as a new marker to monitor the cell status and activities. With the continued development of various SICM based multifunctional imaging methods,[36] we anticipate the wide applications of SICM in interfacial process and cellular biology.

2. Experimental

2.1 Materials and buffer solutions

All chemicals were purchased from Sigma Aldrich and Fisher Chemical, unless mentioned otherwise. All solutions were prepared using deionized water (~18 MΩ) from Ultra Purelab water purification system (ELGA/Siemens). Phosphate buffered saline (PBS) was used as the standard electrolyte solution for the modified PDMS substrates measurements.

2.2 Nanopipette fabrication

The borosilicate glass capillaries (o.d. 1.0 mm, i.d. 0.58 mm; BF100-58-15, Sutter Instrument) were cleaned by piranha solution (3:1 mixture of sulfuric acid and 30% hydrogen peroxide) for 30 minutes prior to use. Nanopipettes were pulled from the cleaned glass capillaries via a P-2000 laser puller (Sutter instrument) with the following parameter: HEAT=275, FIL=4, VEL=50, DEL=225, and PUL=150. Nanopipette tips imaged by a JEOL JSM-6330F scanning electron microscope (SEM) were sputtered with gold (5 nm thickness). Details of the nanopipette characterization are given in Electronic Supplementary Information (ESI).

2.3 SICM setup and approach curve

The SICM (Park System) was placed on a Nikon Eclipse Ti-U inverted microscope, which helps to position the nanopipette, and the optical microscope images were collected by a CCD camera. A flexure guided XY scanner was used for sample positioning and scanning, separated from the topography feedback mechanism of the Z scanner. A glass nanopipette with a tip inner radius about 35 nm was used as the scanning probe. One Ag/AgCl wire electrode (prepared by dipping a 0.2 mm diameter polished Ag wire in bleach for half hour) was inserted in the nanopipette barrel filled with electrolyte, while one Ag/AgCl pellet electrode (Park System) was submerged in the bath solution. Typically, a constant sample bias (V_s) was applied to the bath solution, while the current sensing barrel was connected to a low-noise and high-precision current amplifier with virtual ground. For comparison, a tip bias (V_t) was applied to the nanopipette, and the bath solution was grounded. The single-point approaching current-distance (I-D) curves at different bias polarities and modes were conducted on charged PDMS substrates with an approaching speed of 0.3 μm/s and a large current setpoint (typically 90%). Because of the flexibility of the tip, the slow approaching speed and the softness of the PDMS surface, the tip touches the surface gently. No obvious damage to the tip was noticed based on the measured current and the tip can be used repeatedly.

2.4 SICM imaging

The SICM imaging was conducted in the ARS/hopping mode. For each line scan, the system first finishes a coarse scan (typical 33 points) to assess the overall surface height variation, approaching about 4 μm to reach half of the pre-set setpoint of current change (1%). And then a fine scan (typically 128 points) is implemented. The nanopipette is supposed to stop immediately when the current change exceeds the 2% setpoint. However, because of the time for current averaging (to remove noise) and piezo response, there is typically a small-time delay (<1 ms) for the system to react to stop the tip in our ARS mode.[33, 37] This time delay can induce a large current overshoot, which is typically about 10%, when we use a relatively high approaching speed about 85 μm/s. It should be noted that the time delay is also related to the surface properties such as surface roughness and typically the delay time is longer when the surface is rougher. We therefore need to adjust the imaging parameters for different samples to remain about 10% current change. The typical time traces of tip displacement (Z) and ionic current (I) acquired during coarse and fine scan using positive V_s are shown in Figure S4. The higher current change percentage suggests a smaller minimum D_{ps} ($D_{ps\text{-}min}$) at current $I_{ps\text{-}min}$. In addition, in the fine scan, the nanopipette does not withdraw very far from the surface, which induces the current $I_{ps\text{-}max}$ at $D_{ps\text{-}max}$ is different from the initial current I_0 at initial distance D_0. We defined overall current drop percentage = $(I_0\text{-}I_{ps\text{-}min})/I_0$, fine current decrease $\Delta I_f = I_{ps\text{-}min}\text{-}I_{ps\text{-}max}$ and fine current drop percentage = $\Delta I_f/I_{ps\text{-}max}$. It turns out the ΔI_f and fine current drop percentage are very sensitive to the surface charge. We therefore use the ΔI_f to construct surface charge contrast map. The time traces of Z and I during the SICM imaging were extracted out from the SICM controller through a signal access module and recorded by an oscilloscope (Yokogawa DL850) with a sampling rate of 5 kHz. The bandwidth settings for the Z and I are 500 Hz and 400 Hz, respectively. The ΔI_f based surface charge images were constructed by home-built LabVIEW programs after the topography imaging. It usually takes about 10 min to complete one 10×10 μm image (with 128×128 pixels, unless specified otherwise).

2.5 Cell culture

HeLa cells were cultured in a complete media (mixture of DMEM containing 1% penicillin/streptomycin and 10% fetal bovine serum) in a 5% CO_2 incubator at 37 °C. Cells were seeded at low confluency to allow single-cell measurements. DMSO was added to complete media at different final volume ratio (0%, 0.5%, 1% and 2%). For the transmembrane potential recording, HeLa cells were seeded on a cover glass. For the ΔI_f-based SICM imaging, cells were placed on a collagen hydrogel-modified PDMS substrate in a 40 mm size cell culture petri dish (see the previous report).[21] After 30 min DMSO treatment with different concentrations, the cell samples were rinsed with 1×PBS solution three times. All cell experiments were performed in fresh complete media, while the nanopipettes were also filled with the same media.

2.6 Patch clamp experiments

Transmembrane potential recordings were performed with the current-clamp configuration in whole-cell mode using the Axopatch 200B amplifier (Molecular Devices), and the data was ingested by the software Axoscope 10.5 (Digidata 1440A, Molecular Devices). To avoid cell-to-cell variations, the experiments were repeated three times.

2.7 Data collection and Analysis

The data analysis was carried out by XEI (Park Systems), Gwyddion, LabVIEW (National Instruments), and Origin Pro (OriginLab Corp.). The surface roughness and 3D topography were analyzed by Gwyddion, and the ΔI_f images were constructed by home-built LabVIEW programs.

3. Results and discussion

3.1 Current measurement by SICM

As a scanning probe microscope technique, SICM uses the distance-dependent ion current through the glass nanopipette to record topography.[38] An illustration of SICM setup is shown in Figure 1a (see details in Experimental section). The SEM images of nanopipette tip are shown in Figure 1b, and a nanopore with size about 70 nm can be resolved at the tip in the inset. The ion current across the nanopipette depends upon the electrochemical properties of solution and the geometry of nanopipette tip. The foremost parameter of mapping resolution is the inner radius (r_{pore}) of tip, as the resolution limit has been proved to be approximately $3r_{pore}$.[39]

In experiments, we chose PDMS as the model substrate because it is soft, transparent and biocompatible.[40] PDMS has been widely-used as the substrate and scaffold for cell and tissue studies.[41] To prepare charged surfaces, the flat PDMS substrates were sequentially modified with 3-aminopropyltriethoxysilane (APTES, positively charged at the neutral pH) and bovine serum albumin (BSA, negatively charged at the neutral pH, see details in section ESI-2).[28, 42] To understand the current sensing mechanism, we first controlled the nanopipette to approach to a single point of modified PDMS substrates.[43] Figure 1c shows the typical approaching current-distance (I-D) curves collected on positively charged (black color) and negatively charged (red color) surfaces. A +0.1 V V_s was applied in the bath solution and the current sensing barrel was grounded. When the nanopipette apex is far from the substrate (i.e., 200 nm), the ion current is stable. As the nanopipette tip approaches closer to a substrate, the ion current drops quickly.[44] The overall distance dependent current change can be generally explained by a simplified analytical equation $I(D_{ps})=I_0(1+B/D_{ps})$. B is the geometric factor of the nanopipette tip. I_0 is the initial current as the tip far from the sample, which is mainly determined by the pore resistance (R_{pore}). D_{ps} is the distance between the pipette tip and sample surface.

Because SICM relies on moving ions through the interfacial region between the tip and sample, the influence of the composition of the electrical double layer, a consequence of surface charge can be

investigated.[45] As shown in Figure 1c, the current drops are affected by the surface charge of modified substrates. The percentage of current drop over APTES-PDMS surface was slightly smaller than that over BSA-PDMS surface. With a positive V_s (+0.1 V) applied in the solution, the positive surface charge of the substrate can enlarge the potential difference across the nanopore, thus the ionic flux across the nanopore is enhanced, which slows down the drop of current induced by the decrease of D_{ps}. Near 10% current decrease, the difference of current on positively and negatively charged surfaces is bigger. At higher current drop percentage, the current decrease is slower and the current difference due to surface charge becomes smaller, which may be attributed to the deformation of the PDMS substrate induced by the weak hydrostatic force of the approaching nanopipette.[46] We therefore typically used the near 10% overall current change in the following surface charge contrast mapping on both modified substrates and cell membranes.

We have also conducted systematic tests to collect the ionic current approach curves over charged PDMS substrates using both V_s and V_t modes at ±0.1 V. The outcomes of these tests are shown in Figures 1c, 1d and S2b. As expected, the applied -0.1 V V_s instead produced bigger current change over positively charged surface. In addition, the positive (negative) V_s typically induce similar ion current curves as the positive (negative) V_t, but with opposite polarity dependence of substrate surface charge. In summary, the ionic current change as a function of D_{ps} is always affected by the surface charge of the substrates as well as with the mode and polarity of applied bias. Therefore, we can use the ionic current changes to generate surface charge contrast images.

3.2 FEM simulations

To better understand the experimental results, we simulated the ionic current change over charged surfaces using FEM. The details of FEM simulations can be found in section ESI-4. The nanoprobe was modelled using a two-dimensional axial symmetric geometry, and the nanoprobe was placed at different D_{ps} from a charged surface (Figure S5a). For the case of V_s, a constant bias (±0.1 V) is applied to the bath solution, and the back end of the nanopipette is grounded. For comparison, we also simulated the case of V_t, in which a constant bias (±0.1 V) is applied to the nanopipette while the bath solution is grounded. To simplify the simulation,[47] the finite size of ion and water is ignored, and the system is assumed at a steady state. With these simplifications, the simulation still helps to understand the substrate surface charge induced current changes. Figure S5b showed the distribution of electric potential on a negatively charged surface at V_s of +0.1 V, and the potential is +0.1 V in the bath solution and gradually reduces to zero deep inside the nanopipette.

Figure 2 compared the cation (K^+) concentration profiles and electric field distributions near the nanopipette tip on both negatively (Figures 2a and 2c) and positively charged surface (Figures 2b and 2d) at D_{ps}=35 nm with both V_s bias of +0.1 V (Figures 2a and 2b) and -0.1 V (Figures 2c and 2d). With +0.1 V V_s, the cation concentration in the nanopipette tip region is obviously higher on the positive substrate than on the negative substrate. Correspondingly, the electric fields of the nanopipette tip and the substrate are partially overlapped in the same region on the positive substrate. The cation and electric field results also suggest the higher overlap of diffuse double layer (DDL) of charged surfaces between the nanopipette tip and the positively charged substrate at +0.1 V V_s. As shown in Figures 2c and 2d, the results are the opposite when -0.1 V V_s is applied. Therefore, the ionic flux is always bigger with bigger DDL overlap when the surface charge and applied external potential in the solution have the same polarity to achieve an additive result. These results confirm the ionic flux of nanopipette is sensitive to the surface charge when the D_{ps} is small.

We have simulated the ionic current approach curves over substrates with different surface charge densities by changing the D_{ps} from 400 nm to 35 nm. As shown in Figure 2e, as the D_{ps} decreases, the current change over negatively charged surface is faster and the drop percentage is slightly larger than that over positively charged surface at V_s of +0.1 V. And the applied -0.1 V V_s produced smaller current change over negatively charged surface (Figure 2f). We also simulated the current changes over charged surfaces using V_t biases. The simulated results are shown in Figure S6. When +0.1 V V_s is applied, the cation concentration in the nanopipette tip region is obviously higher on negative substrate, and the electric fields are partially overlapped in the same region. The results are the opposite using -0.1 V V_s. In general, the plot with positive (negative) V_s is similar as the plot with positive (negative) V_t, but with opposite substrate surface charge dependence. Regarding the current changes as a function of D_{ps} on the charged surfaces, the simulated ionic current approach curves support the experimental results we discussed earlier (Figure 1c, 1d and S2b). Although we correctly simulate the trend of current change, the difference of current change and its change percentage is smaller than the experiments. Due to the movement of tip, the fluid near the tip is not steady. The motion of the fluid can reduce the screening effect and enlarge the thickness of diffuse double layer.[48] Therefore, the electroosmotic flow may also play a role in the nanogap region between the tip and the substrate.

3.3 Validation of topographic imaging and surface charge contrast mapping

The topography and surface charge contrast (ΔI_f) images of modified flat PDMS substrates were recorded by the ΔI_f-based SICM method. Figures 3a and 3b show the 3D and 2D topography, respectively, of the BSA modified PDMS substrate using +0.1 V V_s. We quantify the surface roughness by virtue of surface area ratio, which indicates the surface roughness, and the ratio of BSA-PDMS substrate is calculated to be 288.5 in a 10×10 μm^2 area. The overall current drop percentage is about 12% (corresponding to a fine current drop percentage of about 9.0%), which is much bigger than the 2% setpoint. Figure 3c shows the corresponding ΔI_f image in a heatmap form. To better understand the ΔI_f image using ARS mode, the time traces of tip displacement (Z) and ionic current (I), extracted from the sites indicated in Figures 3b and 3c, are presented in Figure 3d. As shown in the Z-t trace, in each pixel of the fine scan, the

nanopipette tip first approached to $D_{ps\text{-}min}$ from the substrate, and then retracted back to $D_{ps\text{-}max}$, followed by a lateral movement (about 78 nm) to the next cycle. The gray dashed line, which followed the lower envelope of the Z-t trace, reflected the height variations on the BSA-PDMS surface. The $D_{ps\text{-}min}$ was controlled reasonably well, and the topography image was acquired without obvious distortions. To evaluate the tip damage, we compared the ionic current traces of coarse scan before and after the BSA-PDMS imaging. As shown in Figure S7, no obvious changes were observed in the ionic current. Because both the PDMS substrate and nanopipette tip are flexible, the tip can still survive the higher current overshooting and finish the imaging. Each pixel in the ΔI_f image was obtained from the current difference ($I_{ps\text{-}min}$-$I_{ps\text{-}max}$) after completing a cycle of tip movement. Because of the height dependency of ion current, the crosstalk between surface charge and height cannot be completely avoided in the ΔI_f image. In general, the ΔI_f is the convolution of both surface charge and height variation. To better understand the extent of the convolution, we investigated both Z and I changes during the fine scan. Compared with the Z changes in Z-t trace, the ΔI_f did not exactly follow the bigger Z changes (red circles) in steep slopes, and bigger ΔI_f appeared in other pixel (blue cycle). Therefore, the ΔI_f does not exactly follow the Z changes. As we will show below, although we cannot quantify the exact surface charge, the ΔI_f image can map the surface charge contrast of modified substrates with heterogenous charge distribution (see sections 3.4 and 3.5).

3.4 Surface charge contrast mapping of flat PDMS substrates

To examine the capability of ΔI_f-based SICM method, we compared the topography and ΔI_f images of both positively and negatively charged PDMS substrates. Figures 4a and 4b show the topography and ΔI_f images of APTES and BSA modified PDMS substrates. The surface roughness of both surfaces is similar with the surface area ratio about 276 and 282, respectively. The values of ΔI_f are always negative using +0.1 V V_s. However, the ΔI_f image of BSA-PDMS surface is generally more negative with an overall green color than that over APTES-PDMS, reflecting its negative surface charge. The drop magnitude of current was impacted by surface charge, and a smaller current change on positive surface than on negative surface was observed. As shown in Figure 4c, the fine current drop is in the range of about 8.5% on the APTES-PDMS surface during fine scan, while the fine current drop is in the range of about 10.6% on the BSA-PDMS. Based on the plot in Figure 1c, the corresponding $D_{ps\text{-}min}$ is about 25 nm and 35 nm, respectively, by means of the overall current drop percentages (about 10.5% and 12.2%). The ΔI_f histograms are constructed with the ΔI_f values at each pixel. As shown in Figure 4d, the negative shift of ΔI_f histogram peak is evident from the -66.41 ± 3.93 pA of APTES-PDMS substrate (i) to the -80.21 ± 7.93 pA of BSA-PDMS substrate (ii). These modifications of PDMS substrates increased the contrast of surface charge without changes of morphology, so the ΔI_f was mainly affected by surface charge.

We have also tested both positive/negative V_s and V_t biases under the same setpoint and other settings. In Figure S8, the value of ΔI_f is positive and the magnitude of ΔI_f on APTES-PDMS surface (76.85 ± 4.40 pA) is much bigger than that on BSA-PDMS surface (62.04 ± 4.71 pA) when using -0.1 V V_s. Therefore, the surface charge difference between APTES and BSA modified PDMS substrates can be differentiated by both V_s polarities. This is the same for the case of V_t biases (see Figures S9 and S10). These results are consistent with the ionic current sensing mechanism we discussed earlier, suggesting that this ΔI_f imaging method can be utilized for surface charge contrast mapping. However, it is worth noting that we typically observed the larger ΔI_f difference using the V_s modes, as the current changes are more pronounced. We thus often use V_s bias for our cell imaging.

3.5 Surface charge contrast mapping of rough Au/PDMS substrates

Having validated the application of ΔI_f-based SICM on flat PDMS surfaces for surface charge contrast mapping, we investigated whether this method could be applied on rough surfaces such as gold coated PDMS (Au/PDMS) substrates. As revealed by SEM images (Figure S3b), the Au/PDMS substrates exhibit complex topographical structures, which are due to the electrochemical etching during gold deposition. The surface area ratio of the Au/PDMS in a 10×10 μm^2 region is around 912. This number is about three times higher than the flat PDMS substrate, confirming the roughness of the Au/PDMS surface. To increase the contrast of surface charge, we modified the Au/PDMS substrates with 4-aminothiophenol (4-ATP) and 4-mercaprobenzoic acid (4-MBA). At neutral pH, the 4-ATP is positively charged, and 4-MBA is negatively charged (see details in section ESI-2).

Figure 5a shows the topography of 4-ATP-Au/PDMS, collected with the mean fine current drop percentage of 3.4% (see Figure 5c, corresponding to an overall current drop percentage of about 9.4%). For the topography of 4-MBA-Au/PDMS in Figure 5b, the mean fine current drop percentage was increased to 8.2% (corresponding to an overall current drop percentage of about 14.1%), provided that the pattern detected varies in height by about 2 μm. The features in the topography images are consistent with the SEM images (Figure S3b), mixed with PDMS and gold regions. The quality of the topography images is slightly lower than the ones we acquired before using potentiometric SICM method.[33] However, the feedback system still works reasonably well even on complicated surfaces. By examining the topography and ΔI_f images, we discovered that the blue and green color points appear around or in nanopits. The lower ΔI_f pixels at these nanopits mean more 4-MBA likely gather in these holes, where more gold depositions happen. These regions are more negative than others, induced by the deprotonated carboxyl groups of 4-MBA molecules. Both the contrast and magnitude of ΔI_f are weaker on positively charged substrate, but stronger on the negatively charged substrate. As shown in Figure S11, the values of ΔI_f became positive, and the magnitude of ΔI_f on positively charged surface is much greater than that on the negatively charged, when a -0.1 V V_s was applied.

Figures S12 and S13 show the topography and ΔI_f images of 4-ATP and 4-MBA modified Au/PDMS substrates with V_t biases. Using +0.1 V V_t, blue color regions appear in the ΔI_f image of 4-ATP-

Au/PDMS. These blue color regions are mostly deposited with gold, suggesting the 4-ATP modified gold surface is more positive than the 4-MBA modified surface. The ΔI_f images are also sensitive to the surface charge using -0.1 V V_t, as the values of ΔI_f on positively charged surface are smaller than that on negatively charged surface. The surface charge features on rough substrates can be detected, which are proved by both V_s and V_t modes. These observations follow the same trend in flat surfaces results, which further substantiate that we can qualitatively map the surface charge contrast of heterogeneous surface using the ΔI_f-based SICM method.

3.6 Simultaneous topography and surface charge contrast mapping of live HeLa cells

We then used this ΔI_f-based SICM method to image live cell surface. To induce surface charge changes to cell membrane, the cells were treated with elevated level of DMSO, which can induce transient or permanent changes and damages to the cell membranes.[49] It has also demonstrated that DMSO can alter the elasticity of the membrane, even at a relatively low DMSO concentration.[50] Transmembrane potential measurements were applied to assess the short-term effect of DMSO treatment of HeLa cells. In the optical microscope images (Figure S14a), no apparent cell morphological deformations were observed right after 30 min of DMSO treatment with different concentrations (v/v, 0%, 0.5%, 1% and 2%). However, the recorded transmembrane potentials became less negative with the increase of extracellular DMSO concentration, as shown in Figure S14b. The depolarized cell membrane confirmed that small cell membrane damages occurred after the DMSO treatment. We focused on the cells treated by 1% DMSO in the following SICM imaging.

For ΔI_f-based SICM imaging, the HeLa cells were seeded on PDMS substrate modified with collagen hydrogel, which provides a favourable local environment and protects the nanopipette tip.[21] Figures 6a-f show the topography and ΔI_f images of untreated cell and cell after 1% DMSO treatment using +0.1 V V_s (20×10 μm, with 128×64 pixels). The white and black solid lines in the topography and ΔI_f images, respectively, indicate the boundary between the cell and collagen hydrogel matrix. By comparing the 3D and 2D topography images of untreated and treated cells, no noticeable differences can be observed. However, we are not able to tell if there are differences in more detailed subcellular cell membrane structures due to the limited spatial resolution.[37] The surface roughness analysis suggests that the surface area ratio of HeLa cell treated with 1% DMSO is about 179.9 in a 10×10 μm^2 area, which is slightly larger than the typical value around 154 for the untreated cells. Therefore, the 1% DMSO treatment only made the cell membrane slightly rougher, which is attributed to the reorganization of lipid, proteins and actin filament of cell membrane. The surfaces of both untreated and treated cells are much smoother than the Au/PDMS substrates.

Because the relatively smooth surface and expansion of scanning range, the $D_{ps\text{-}min}$ is better-controlled, and the mean fine current drop percentage is only about 2.4% (an overall current drop percentage of about 8.4%). The current change is slightly bigger on the 1% DMSO-treated cell, with the mean fine current drop of about 4.0%. Both values are much smaller than that on the modified PDMS and Au/PDMS substrates, resulting in the much smaller ΔI_f magnitude. As shown in both ΔI_f images in Figures 6c and 6f, the collagen hydrogel modified PDMS surface (orange/blue regions) is more positive than the cell surface. This is consistent with the results taken by potentiometric SICM method using a dual-barrel nanopipette.[21] The ΔI_f values were generally homogeneous on the untreated cell and no obvious heterogeneities were observed (see Figure 6c). The overall color of the ΔI_f image on the treated cell surface (see Figure 6f) turns to green/bule, suggesting a more negative surface. In addition, we observed several blue dots with deep blue color (more negative) in Figure 6f, which may be attributed to the damage sites of cell membrane. Figure 6g reveals the mean ΔI_f is -32.54 pA for the treated HeLa cell, which is more negative than that of the untreated cell (-19.07 pA). In contrast to the noticeable changes of ΔI_f values between untreated and treated cell surfaces, the ΔI_f values are similar on the collagen matrix regions at the corners in the ΔI_f images. Therefore, the 1% DMSO treatment has negligible impact on the collagen matrix. As seen from Figure 6h (i, ii), the representative time traces of Z movement and I along the black and blue dashed lines in the 3D topography and ΔI_f images exhibited the detailed changes of height and ion current across the cell membrane and collagen-modified PDMS surface. Compared with Z, significant variations of ΔI_f have been observed, and the ΔI_f changes do not exactly follow the changes in the Z-t trace. The very different responses of Z and I confirm that the ΔI_f is mainly affected by factors other than the Z changes, and the surface charge variation should play an important role.

The surface charge of live cell membrane is mainly attributed to the electrostatic charges carried by biomolecules, such as lipids and proteins. The DMSO treatment induced the composition and structural changes of cell membrane, likely introducing more negative charges to the membrane surface. The surface damages also induce a higher permeability of the cell membrane, which can expose the more negative interior and allow the release of more cellular contents.[51] Bigger ion flux is expected through damaged sites, which can induce more changes in ion concentration and local potential distributions near the membrane. These changes can lead to an apparently more negative cell surface after the 1% DMSO treatment.

4. Conclusions

In this work, we proposed a potent ΔI_f-based SICM method for recording the topography and revealing surface charge contrast of soft substrates in solution and applied it to membranes of live cells. With a relatively fast scanning speed, the actual current change is larger and the D_{ps} is smaller than the values of typical SICM imaging condition. Therefore, the nanopipette tip often experiences stronger interactions with the substrate and may be damaged by the rigid surface. However, the method works well on soft substrates and the acquired topography images show reasonable quality. Importantly, although we cannot avoid the crosstalk between topographic and surface charge changes, we found an improved correlation between the percentage of ionic current change and the charge polarity of

substrate during scanning. The ΔI_f shows significant differences between the positively and negatively charged substrates with similar topographic features, and the trend is supported by the FEM simulation. Furthermore, significant difference in the magnitude of ΔI_f has been found between the native cell and the cell after 1% DMSO treatment. The observed differences are attributed to the surface charge changes induced by small cell membrane damages right after DMSO treatment. Compared with the voltage sensitive dye-based fluorescence microscope technique, the ΔI_f images by SICM can map surface charge contrast of non-labelled living cell membranes with a high spatial resolution. Compared with the potentiometric SICM method using double-barrel nanopipette, the quality (*i.e.*, spatial resolution) of topography images acquired by the ΔI_f method is slightly reduced and the surface charge measurement is less accurate. However, this method is simpler in operation and faster in imaging speed. In summary, we have developed a simple SICM based surface charge contrast mapping method, which can be a powerful technique for qualitatively mapping of surface charge changes of complexed living cell membranes. Acquiring changes in topography and surface charge distribution simultaneously is advantageous for studying the physiology and bioelectrical properties of soft live cell membranes. This SICM method can complement the voltage-sensitive fluorescence imaging techniques to provide high spatial resolution and measure long-term electrical changes of live cells.

Conflicts of interest

There are no conflicts to declare.

Acknowledgements

Authors gratefully thank for the supports by grants from National Natural Science Foundation of China (62001239 and 81771980) and National Science Foundation (CBET1454544).

Notes and references

1. M. Levin and C. G. Stevenson, *Annual Review of Biomedical Engineering*, 2012, **14**, 295-323.
2. D. Adams and M. Levin, *Cell and Tissue Research*, 2012, 1-28.
3. D. J. Blackiston, K. A. McLaughlin and M. Levin, *Cell cycle (Georgetown, Tex.)*, 2009, **8**, 3519-3528.
4. D. S. Adams and M. Levin, *Cold Spring Harbor Protocols*, 2012, **2012**, pdb.top067710.
5. W. Zhao, W. Cui, S. Xu, L.-Z. Cheong, D. Wang and C. Shen, *Nanoscale Advances*, 2019, **1**, 537-545.
6. E. Drolle, W. Ngo, Z. Leonenko, L. Subbaraman and L. Jones, *Translational vision science & technology*, 2020, **9**, 41.
7. N. S. Malvankar, S. E. Yalcin, M. T. Tuominen and D. R. Lovley, *Nature nanotechnology*, 2014, **9**, 1012-1017.
8. A. Dols-Perez, G. Gramse, A. Calo, G. Gomila and L. Fumagalli, *Nanoscale*, 2015, **7**, 18327-18336.
9. K. Jang, J. Choi, C. Park and S. Na, *Biosensors & bioelectronics*, 2017, **87**, 222-228.
10. S. Chen, H. Dong and J. Yang, *Sensors*, 2020, **20**.
11. P. Hansma, B. Drake, O. Marti, S. Gould and C. Prater, *Science*, 1989, **243**, 641 - 643.
12. Y. E. Korchev, M. Milovanovic, C. L. Bashford, D. C. Bennett, E. V. Sviderskaya, I. Vodyanoy and M. J. Lab, *Journal of Microscopy*, 1997, **188**, 17-23.
13. J. Gorelik, A. I. Shevchuk, G. I. Frolenkov, I. A. Diakonov, M. J. Lab, C. J. Kros, G. P. Richardson, I. Vodyanoy, C. R. W. Edwards, D. Klenerman and Y. E. Korchev, *Proceedings of the National Academy of Sciences*, 2003, **100**, 5819-5822.
14. J. Gorelik, Y. Zhang, A. I. Shevchuk, G. I. Frolenkov, D. Sánchez, M. J. Lab, I. Vodyanoy, C. R. W. Edwards, D. Klenerman and Y. E. Korchev, *Molecular and Cellular Endocrinology*, 2004, **217**, 101-108.
15. J. Rheinlaender and T. E. Schaffer, *Nanoscale*, 2019, **11**, 6982-6989.
16. A. Gesper, P. Hagemann and P. Happel, *Nanoscale*, 2017, **9**, 14172-14183.
17. Y. Shan, N. Panday, Y. Myoung, M. Twomey, X. Wang, W. Li, E. Celik, V. Moy, H. Wang, J. H. Moon and J. He, *Macromolecular Bioscience*, 2016, **16**, 599-607.
18. A. I. Shevchuk, P. Hobson, M. J. Lab, D. Klenerman, N. Krauzewicz and Y. E. Korchev, *Biophysical journal*, 2008, **94**, 4089-4094.
19. W. Shin and K. D. Gillis, *Biophysical journal*, 2006, **91**, L63-L65.
20. E. Tognoni, *Current Opinion in Electrochemistry*, 2021, **28**, 100738.
21. F. Chen, P. Manandhar, M. S. Ahmed, S. Chang, N. Panday, H. Zhang, J. H. Moon and J. He, *Macromolecular Bioscience*, 2019, **19**, 1800271.
22. J. Rheinlaender, N. A. Geisse, R. Proksch and T. E. Schäffer, *Langmuir : the ACS journal of surfaces and colloids*, 2010, **27**, 697-704.
23. M. Miragoli, A. Moshkov, P. Novak, A. Shevchuk, V. O. Nikolaev, I. El-Hamamsy, C. M. F. Potter, P. Wright, S. H. S. A. Kadir, A. R. Lyon, J. A. Mitchell, A. H. Chester, D. Klenerman, M. J. Lab, Y. E. Korchev, S. E. Harding and J. Gorelik, *Journal of The Royal Society Interface*, 2011, **8**, 913-925.
24. D. Perry, A. Page, B. Chen, B. G. Frenguelli and P. R. Unwin, *Analytical chemistry*, 2017, **89**, 12458-12465.
25. A. Page, D. Perry, P. Young, D. Mitchell, B. G. Frenguelli and P. R. Unwin, *Analytical chemistry*, 2016, **88**, 10854-10859.
26. V. Shkirskiy, M. Kang, I. J. McPherson, C. L. Bentley, O. J. Wahab, E. Daviddi, A. W. Colburn and P. R. Unwin, *Analytical chemistry*, 2020, **92**, 12509-12517.
27. C. Zhu, G. Jagdale, A. Gandolfo, K. Alanis, R. Abney, L. Zhou, D. Bish, J. D. Raff and L. A. Baker, *Environmental science & technology*, 2021, **55**, 12233-12242.
28. K. McKelvey, S. L. Kinnear, D. Perry, D. Momotenko and P. R. Unwin, *Journal of the American Chemical Society*, 2014, **136**, 13735-13744.
29. D. Perry, B. Paulose Nadappuram, D. Momotenko, P. D. Voyias, A. Page, G. Tripathi, B. G. Frenguelli and P. R. Unwin, *Journal of the American Chemical Society*, 2016, **138**, 3152-3160.
30. K. Cremin, B. A. Jones, J. Teahan, G. N. Meloni, D. Perry, C. Zerfass, M. Asally, O. S. Soyer and P. R. Unwin, *Analytical chemistry*, 2020, **92**, 16024-16032.
31. L. H. Klausen, T. Fuhs and M. Dong, *Nature communications*, 2016, **7**, 12447.

32. Y. Zhou, C.-C. Chen, A. E. Weber, L. Zhou and L. A. Baker, *Langmuir : the ACS journal of surfaces and colloids*, 2014, **30**, 5669-5675.
33. F. Chen, N. Panday, X. Li, T. Ma, J. Guo, X. Wang, L. Kos, K. Hu, N. Gu and J. He, *Nanoscale*, 2020, **12**, 20737-20748.
34. P. Novak, C. Li, A. Shevchuk, R. Stepanyan, M. Caldwell, S. Hughes, T. Smart, J. Gorelik, V. Ostanin, M. Lab, G. Moss, G. Frolenkov, D. Klenerman and Y. Korchev, *Nature methods*, 2009, **6**, 279 - 281.
35. T. Ushiki, M. Nakajima, M. Choi, S. J. Cho and F. Iwata, *Micron*, 2012, **43**, 1390-1398.
36. A. Page, D. Perry and P. R. Unwin, *Proceedings of the Royal Society A: Mathematical, Physical and Engineering Science*, 2017, **473**.
37. G.-E. Jung, H. Noh, Y. K. Shin, S.-J. Kahng, K. Y. Baik, H.-B. Kim, N.-J. Cho and S.-J. Cho, *Nanoscale*, 2015, **7**, 10989-10997.
38. N. Taira, Y. Nashimoto, K. Ino, H. Ida, T. Imaizumi, A. Kumatani, Y. Takahashi and H. Shiku, *Analytical chemistry*, 2021, **93**, 4902-4908.
39. P. Hagemann, A. Gesper and P. Happel, *ACS Nano*, 2018, **12**, 5807-5815.
40. J. Nedoma, M. Fajkus, L. Bednarek, J. Frnda, J. Zavadil and V. Vasinek, *Advances in Electrical and Electronic Engineering*, 2016, **14**.
41. A. Gokaltun, Y. B. A. Kang, M. L. Yarmush, O. B. Usta and A. Asatekin, *Scientific reports*, 2019, **9**, 7377.
42. Z. G. Peng, K. Hidajat and M. S. Uddin, *J Colloid Interface Sci*, 2004, **271**, 277-283.
43. Y. Jiao, J. Zhuang, T. Zhang and L. He, *Analytical chemistry*, 2021, **93**, 12296-12304.
44. D. Sánchez, N. Johnson, C. Li, P. Novak, J. Rheinlaender, Y. Zhang, U. Anand, P. Anand, J. Gorelik, G. I. Frolenkov, C. Benham, M. Lab, V. P. Ostanin, T. E. Schäffer, D. Klenerman and Y. E. Korchev, *Biophysical journal*, 2008, **95**, 3017-3027.
45. C. Zhu, K. Huang, N. P. Siepser and L. A. Baker, *Chemical reviews*, 2020.
46. M. Pellegrino, P. Orsini, M. Pellegrini, P. Baschieri, F. Dinelli, D. Petracchi, E. Tognoni and C. Ascoli, *Neuroscience Research*, 2011, **69**, 234-240.
47. N. Panday, G. Qian, X. Wang, S. Chang, P. Pandey and J. He, *ACS Nano*, 2016, **10**, 11237-11248.
48. J. Teahan, D. Perry, B. Chen, I. J. McPherson, G. N. Meloni and P. R. Unwin, *Analytical chemistry*, 2021, **93**, 12281-12288.
49. R. Notman, M. Noro, B. O'Malley and J. Anwar, *Journal of the American Chemical Society*, 2006, **128**, 13982-13983.
50. B. Gironi, Z. Kahveci, B. McGill, B. D. Lechner, S. Pagliara, J. Metz, A. Morresi, F. Palombo, P. Sassi and P. G. Petrov, *Biophysical journal*, 2020, **119**, 274-286.
51. Y. Zhou, C.-O. Wong, K.-j. Cho, D. van der Hoeven, H. Liang, D. P. Thakur, J. Luo, M. Babic, K. E. Zinsmaier, M. X. Zhu, H. Hu, K. Venkatachalam and J. F. Hancock, *Science*, 2015, **349**, 873-876.

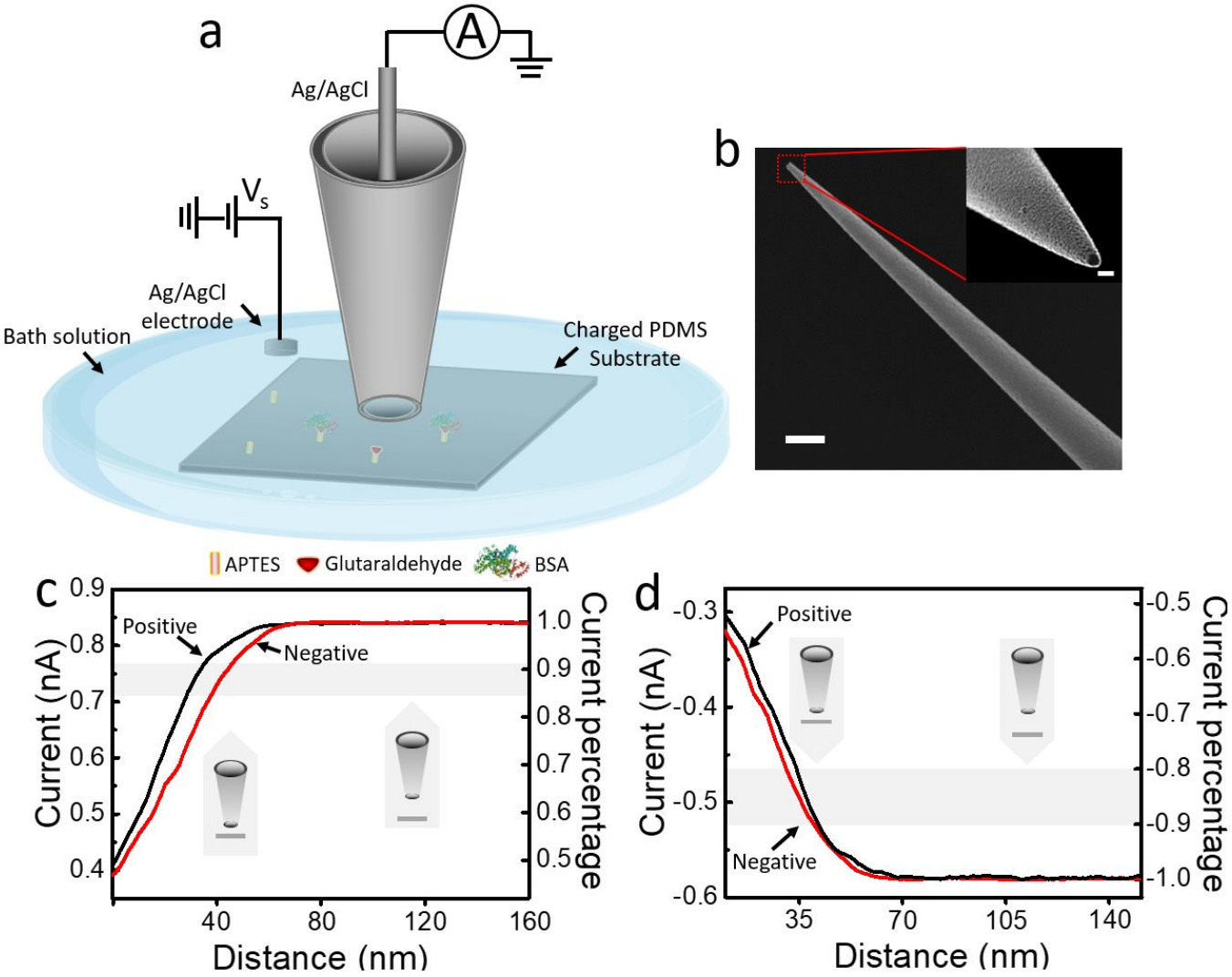

Figure 1. Simultaneous topographical mapping and surface charge contrast imaging by the ΔI_f-based SICM. **(a)** Schematic of the SICM configuration with a borosilicate glass nanopipette as probe. **(b)** The side-view SEM image (scale bar, 1 μm) and end-view SEM image (scale bar, 100 nm) of a typical SICM nanopipette tip. **(c-d)** Typical approaching I-D curves for ionic current on a positively charged substrate (APTES-PDMS, black) and a negatively charged substrate (BSA-PDMS, red) in 1×PBS buffer using +0.1V V_s **(c)** and -0.1V V_s **(d)**. The grey range indicates the current change used for surface charge contrast mapping.

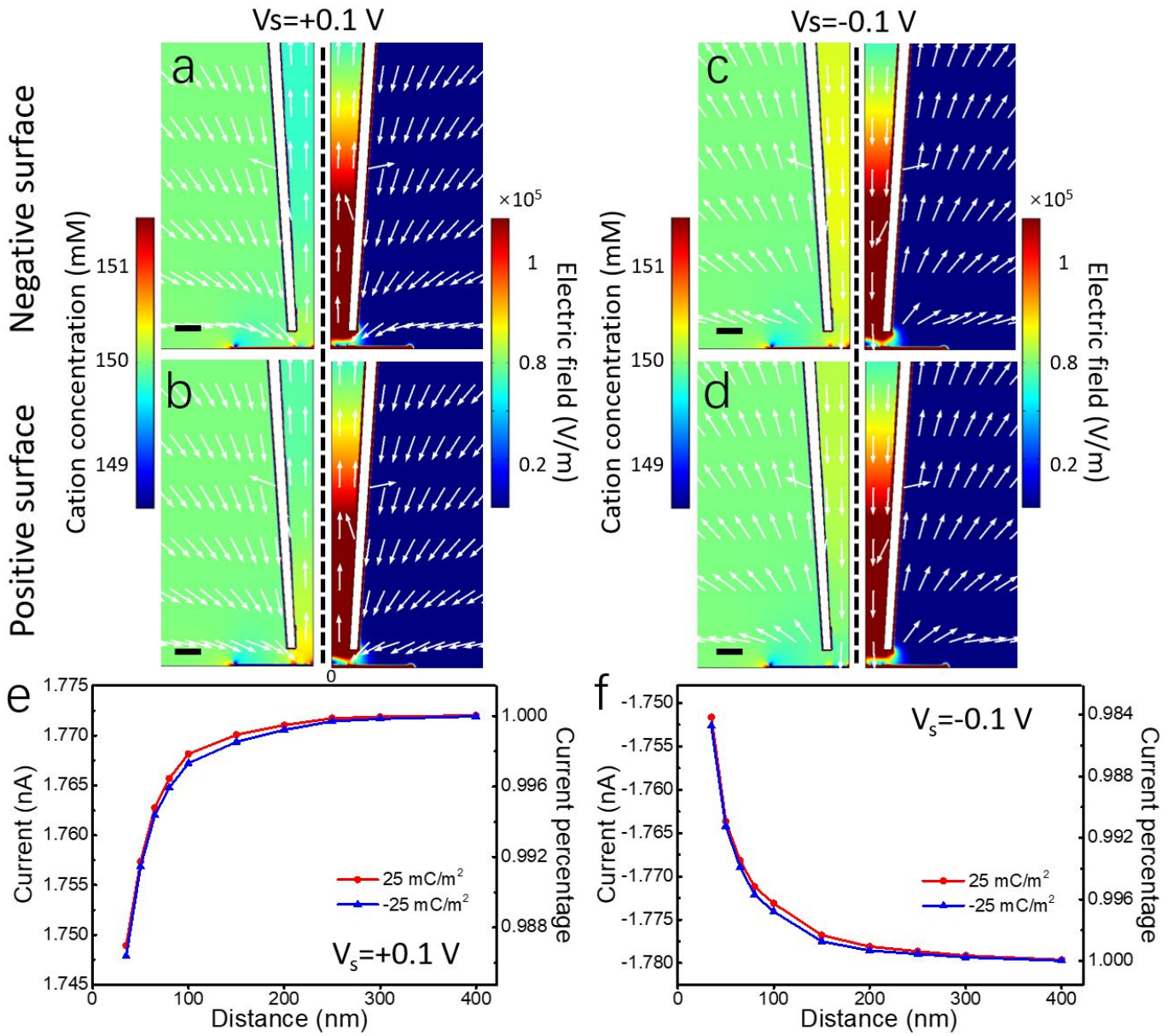

Figure 2. (a-d) FEM simulation results of cation concentration (on the left of each subsection) and electric field distribution (on the right of each subsection) near the tip of negatively charged nanopipette over different charged substrates using V_s biases (scale bar: 50 nm). Data are obtained from a negatively charged surface (-25 mC/m^2) at D_{ps}=35 nm using +0.1 V V_s **(a)** and -0.1 V V_s **(c)**; a positively charged surface (25 mC/m^2) at D_{ps}=35 nm using +0.1 V V_s **(b)** and -0.1 V V_s **(d)**. The mass-transport of the cations and the direction of the electric field are denoted with white arrows. **(e-f)** The simulated current changes versus D_{ps} using V_s=+0.1 V **(e)** and V_s=-0.1 V **(f)**.

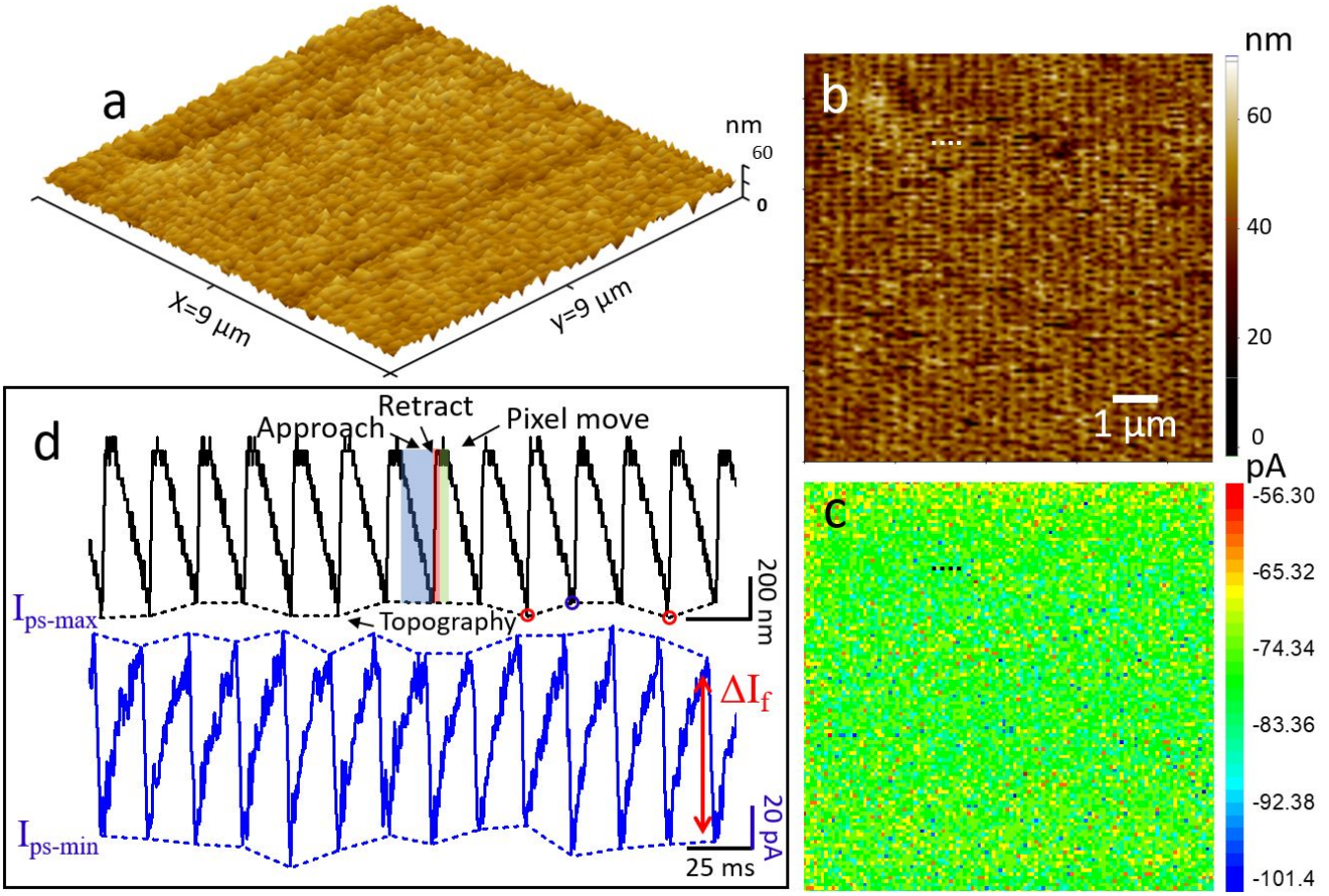

Figure 3. Simultaneously recorded topography and ΔI_f images of BSA-PDMS substrate. **(a-b)** The 3D and 2D topography images. **(c)** The corresponding ΔI_f image. **(d)** The time traces of Z movement (black) and ion current (blue) indicated in **(b)** and **(c)**. The blue, red, and green shaded regions in Z-t trace indicating the approach, retract, and pixel move. All images were recorded in 1×PBS buffer using +0.1 V V_s.

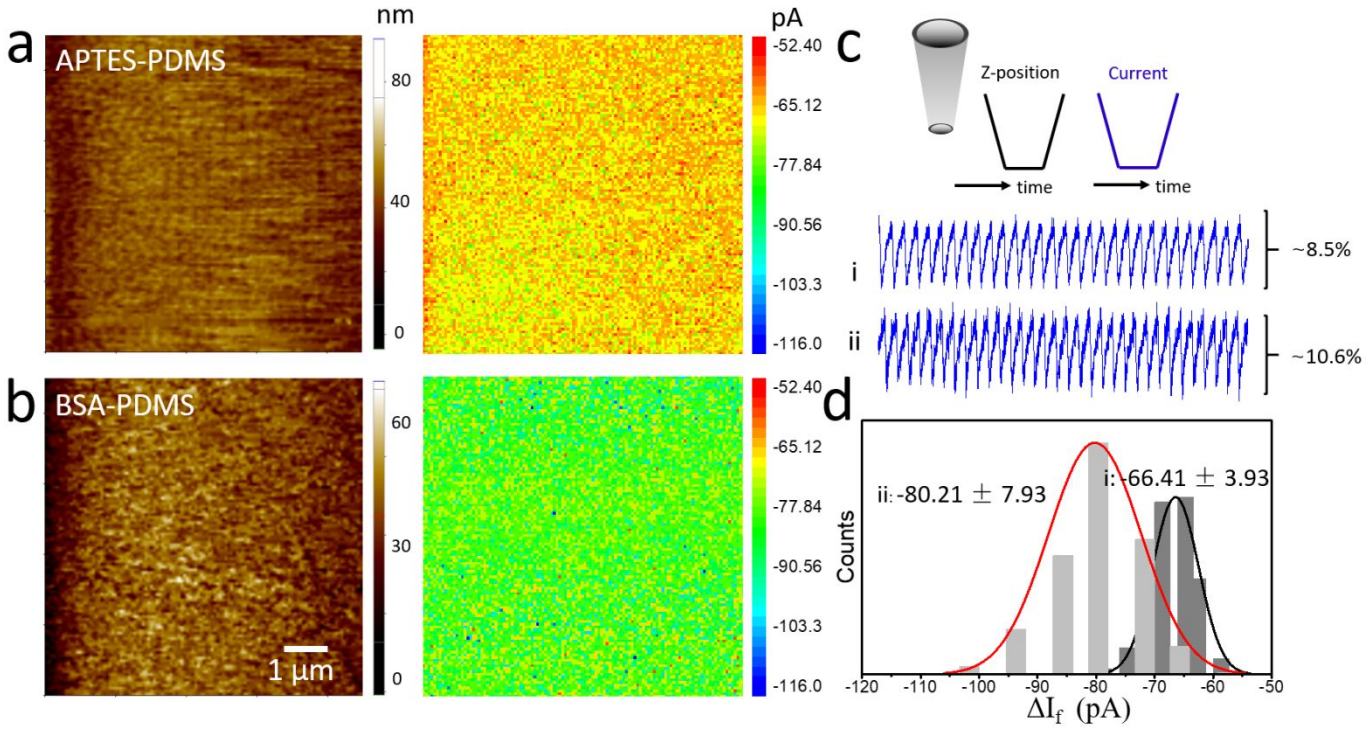

Figure 4. (a-b) The representative topography (left) and surface charge (ΔI_f) contrast images (right) of PDMS substrates modified with APTES **(a, positively charged)** and BSA **(b, negatively charged)** using +0.1 V V_s. **(c-d)** The typical I_f time traces **(c)** and the ΔI_f histograms **(d)** on APTES-PDMS (i) and BSA-PDMS (ii) substrates. All images were recorded in 1×PBS buffer.

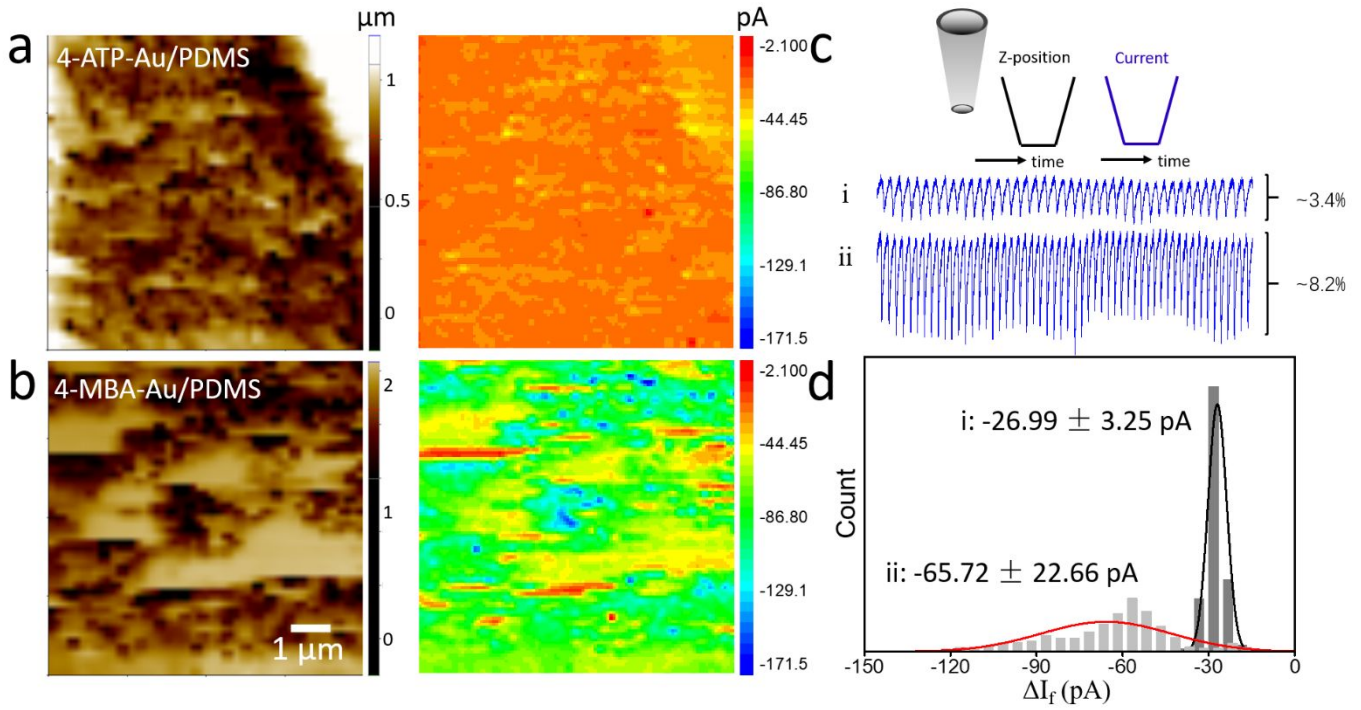

Figure 5. (a-b) The representative topography (left) and surface charge (ΔI_f) contrast images (right) of Au/PDMS substrates modified with 4-ATP **(a, positively charged)** and 4-MBA **(b, negatively charged)** using +0.1 V V_s. **(c-d)** The typical I_f time traces **(c)** and the ΔI_f histograms **(d)** on 4-ATP-Au/PDMS (i) and 4-MBA-Au/PDMS (ii) substrates. All images were recorded in 1×PBS buffer.

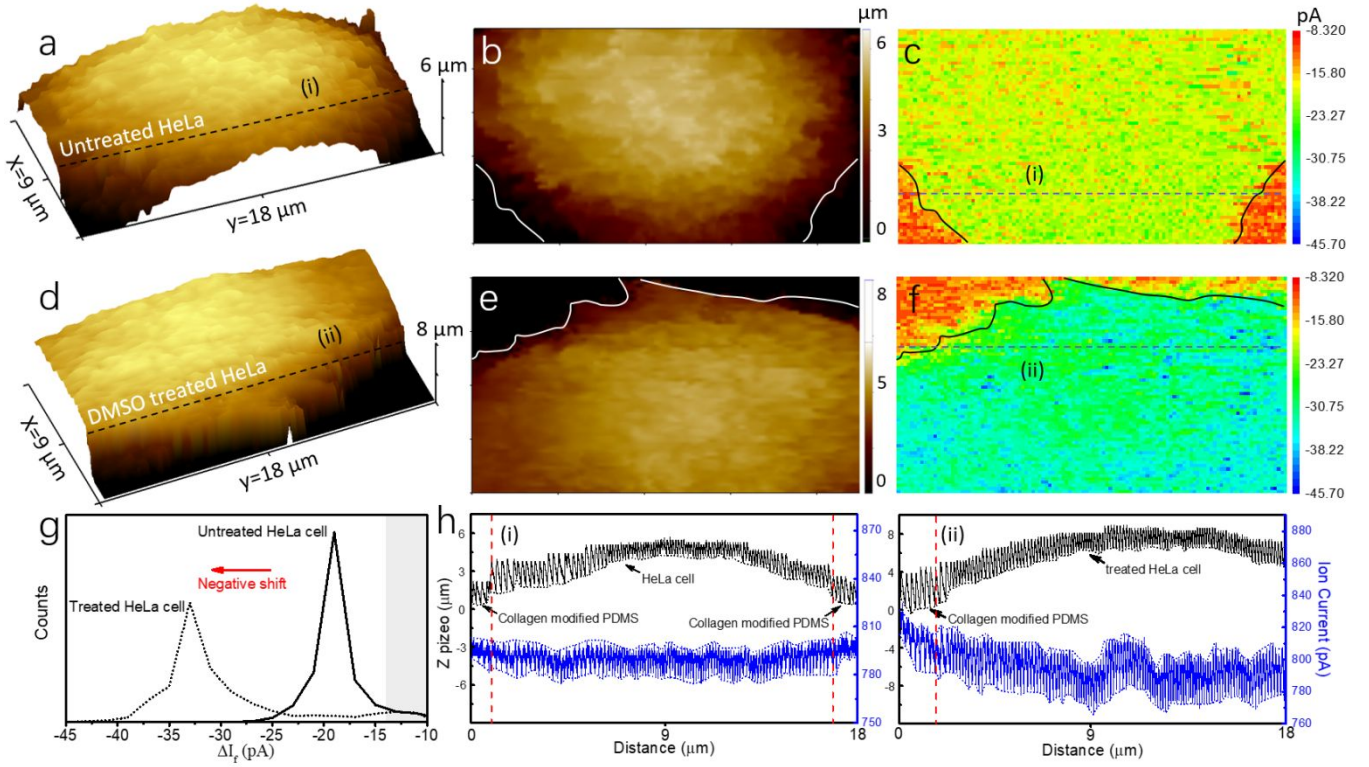

Figure 6. Simultaneous topography and surface charge (ΔI_f) contrast images of untreated and treated HeLa cells after 1% DMSO treatment. **(a-b)** The 3D and 2D topography images of an untreated cell. **(c)** The corresponding ΔI_f image. **(d-e)** The 3D and 2D topography images of a treated cell. **(f)** The corresponding ΔI_f image. The white and black solid lines in 2D topography and ΔI_f images indicate the edge of cell. **(g)** The ΔI_f histograms are constructed from the whole ΔI_f images in **(c)** and **(f)**, and the gray region indicates the ΔI_f distributions of the collagen hydrogel on PDMS substrates. **(h)** Simultaneously recorded time traces of Z (black) and ion current I (blue) through the black and blue dashed lines of the untreated **(a, c)** and treated cells **(d, f)**. All the images were recorded in fresh complete media using +0.1 V V_s.